ADVANCED FUNCTIONAL MATERIALS
www.afm-journal.de

Improved Solubility in Metavalently Bonded Solid Leads to Band Alignment, Ultralow Thermal Conductivity, and High Thermoelectric Performance in SnTe

Yuqi Liu, Xuemei Zhang, Pengfei Nan, Bo Zou, Qingtang Zhang, Yunxiang Hou, Shuang Li, Yaru Gong, Qingfeng Liu, Binghui Ge, Oana Cojocaru-Mirédin, Yuan Yu, Yongsheng Zhang,* Guang Chen, Matthias Wuttig,* and Guodong Tang**

SnTe is an emerging Pb-free thermoelectric compound that has drawn significant attention for clean energy conversion. Chemical doping is routinely used to tailor its charge carrier concentration and electronic band structures. However, the efficacy of dopants is often limited by their small solubility. For example, only 0.5% Ag can be incorporated into the SnTe matrix. Yet, significantly more Ag (>7%) can be dissolved if SnTe is alloyed with $AgSbTe_2$. This large enhancement of solubility can be understood from a chemical bonding perspective. Both SnTe and $AgSbTe_2$ employ metavalent bonding as identified by an unusual bond-rupture in atom probe tomography. Density functional theory calculations show that upon Ag doping the energy offset of the upmost two valence bands decreases significantly. This induces band alignment in SnTe, which results in an enhanced power factor over a broad temperature range. Moreover, the increased concentration of point defects and associated lattice strain lead to strong phonon scattering and softening, contributing to an extremely low κ_L of 0.30 $Wm^{-1}K^{-1}$. These synergistic effects contribute to a peak *ZT* of 1.8 at 873 K and a record-high average *ZT* of ≈1.0 between 400 and 873 K in $Sn_{0.87}Mn_{0.08}Sb_{0.08}Te$–5%$AgSbTe_2$ alloy.

1. Introduction

Thermoelectric materials can convert waste heat into electricity without mechanical transmission, noise, or pollution.[1–3] They are considered potential candidates to realize a more sustainable source of energy. The energy conversion efficiency of thermoelectric devices is related to the temperature difference between the cold–hot end and the thermoelectric figure of merit *ZT*, defined as $ZT = (S^2\sigma/\kappa_T)T$, where *S*, σ, κ_T, and *T* are the Seebeck coefficient, the electrical conductivity, the total thermal conductivity, and the absolute temperature, respectively.[4] κ_T consists of the electronic thermal conductivity (κ_e) and the lattice thermal conductivity (κ_L). The Seebeck coefficient and electrical conductivity are governed by the carrier concentration, which can be

Y. Liu, B. Zou, Q. Zhang, Y. Hou, S. Li, Y. Gong, G. Chen, G. Tang
MIIT Key Laboratory of Advanced Metallic and Intermetallic Materials Technology
School of Materials Science and Engineering
Nanjing University of Science and Technology
Nanjing 210094, China
E-mail: tangguodong@njust.edu.cn

X. Zhang, Y. Zhang
Key Laboratory of Materials Physics
Institute of Solid State Physics
Chinese Academy of Sciences
Hefei 230031, China
E-mail: yshzhang@theory.issp.ac.cn

The ORCID identification number(s) for the author(s) of this article can be found under https://doi.org/10.1002/adfm.202209980.

DOI: 10.1002/adfm.202209980

P. Nan, B. Ge
Key Laboratory of Structure and Functional Regulation of Hybrid Materials of Ministry of Education
Institutes of Physical Science and Information Technology
Anhui University
Hefei 230601, China

Q. Liu
State Key Laboratory of Materials-Oriented Chemical Engineering
College of Chemical Engineering
Nanjing Tech University
Nanjing 210009, China

O. Cojocaru-Mirédin, Y. Yu, M. Wuttig
Institute of Physics (IA)
RWTH Aachen University
52056 Aachen, Germany
E-mail: yu@physik.rwth-aachen.de; wuttig@physik.rwth-aachen.de

Y. Zhang
Advanced Research Institute of Multidisciplinary Sciences
Qufu Normal University Qufu
Shandong 273165, China

M. Wuttig
Peter Grünberg Institute—JARA-Institute Energy-Efficient Information Technology (PGI-10)
Forschungszentrum Jülich GmbH
52428 Jülich, Germany

controlled by doping.[5] In recent years it has been realized that doping can play a much more prominent role, since it can also tailor the band structure and thus the effective mass of charge carriers.[6–9] To obtain pronounced changes in the electronic band structure, a significant level of doping is required. This is no simple task to accomplish, since often limited dopant solubilties restrict the desired property improvement.

SnTe is a promising thermoelectric alternative to PbTe by replacing the toxic Pb with environmentally friendly Sn.[10] Various methods such as tuning the carrier concentration, engineering the energy band structures, and introducing structural defects have been utilized to optimize the thermoelectric properties of SnTe.[11] Nevertheless, the resulting performance is still inferior to the PbTe-based compounds, diminishing the benefit of SnTe for practical applications. The lower *ZT* values of SnTe are in part due to differences in the electronic structure. Even though SnTe employs the same rock-salt structure and similar electronic band structures as PbTe,[12] a much smaller bandgap (0.18 eV at 300 K) and larger energy offset (0.3–0.4 eV) between the light-hole band (L band) and a heavy-hole band (Σ band) are observed in SnTe.[13,14] These factors lead to poor Seebeck coefficients and inferior thermoelectric performance.

The energy offset between the light and heavy valence bands can be reduced through band convergence. It was demonstrated that doping with Mg,[15] Hg,[16] Cd,[17] and Ca[18] can narrow the energy offset and enlarge the direct bandgap of SnTe. Nevertheless, this offset value is still larger than 0.1–0.2 eV due to the limited solubility of these elements in SnTe.[15,17] This impedes further optimization of the Seebeck coefficient and the power factor. Ag has also emerged as an environment-benign dopant to assist the valence band convergence.[19–21] Yet, the solubility limit of Ag in SnTe is extremely low, which is ≈0.5 at.%.[22] This small solubility significantly reduces the efficacy of Ag in promoting band convergence. Enhancing the solubility of adequate dopants is thus mandatory to further reduce the energy offset and thus realize improved band convergence.[23] According to the Hume–Rothery rule, the solubility limit of dopants is governed by the atomic size and electronegativity of solute and solvent.[24] Additionally, manipulating configurational entropy[25] and processing under non-equilibrium conditions[26] were proposed to improve the solubility of dopants. Yet, it is still difficult to identify suitable dopants fulfilling the rules outlined above. A time-consuming "trial and error" method is thus often necessary. It is, therefore, highly desirable to identify or even better predict dopants with high solulibility limits.

In this work, we demonstrate that the solubility of dopants can be greatly influenced by the chemical bonding mechanisms of the alloying compounds. While only 0.5% Ag can be incorporated into the SnTe matrix, significantly more Ag (>7%) can be dissolved if SnTe is alloyed with $AgSbTe_2$. This striking difference in solubility cannot be explained by the Hume–Rothery rule but originates from the similarities in the chemical bonds locally formed. The improved solubility also leads to band alignment between light and heavy valence bands and strong phonon scattering, giving rise to a remarkable peak *ZT* value of 1.8 at 873 K and a record-high average *ZT* of ≈1.0 between 400 and 873 K in SnTe. Our work provides a new avenue to improve the solubility of dopants, which is even important for semiconductors beyond thermoelectrics.

2. Results and Discussion

2.1. The Improved Solubility Limit of Dopants in Metavalently Bonded Solids

Powder X-ray diffraction (XRD) patterns of $Sn_{1.03-2x}Mn_xSb_xTe$ samples (Figure S1a, Supporting Information) reveal a single phase that can be indexed to rock-salt SnTe (PDF #46-1210, Fm-3m space group). The (200) diffraction peaks shift to a high angle with increasing the doping content, giving rise to a contraction in the lattice constants extracted from Rietveld refinement (Figure S2, Supporting Information) induced by Mn and Sb codoping (Figure S1b, Supporting Information). This can be attributed to the smaller ionic radius of Mn^{2+} (0.67 Å) and Sb^{3+} (0.76 Å) in contrast to Sn^{2+} (0.93 Å). Rietveld-refined XRD patterns and the refinement details of one example can be found in Figure S2 and Table S3 (Supporting Information), respectively. After alloying $AgSbTe_2$ into $Sn_{0.87}Mn_{0.08}Sb_{0.08}Te$, the XRD patterns are still consistent with the rock-salt structure of SnTe (Figure S1c, Supporting Information). The lattice parameters decrease with increasing $AgSbTe_2$ content (Figure S1d, Supporting Information), which is in agreement with the difference in the lattice parameters between NaCl-structured $Sn_{0.87}Mn_{0.08}Sb_{0.08}Te$ (6.3093 Å) and $AgSbTe_2$ (6.079 Å) and the Vegard's law.[27] No secondary phase can be detected within the detection limit of laboratory XRD and energy dispersive spectroscopy (EDS) attached to a scanning electron microscope (SEM) in both $Sn_{0.87}Mn_{0.08}Sb_{0.08}Te$ and $AgSbTe_2$-alloyed samples (Figures S3, S4, Supporting Information), indicating that the solid solubility limit of Ag in SnTe has been increased to beyond 7% in our design. Atomic-resolution high-angle annular dark-field scanning transmission electron microscopy (HAADF-STEM) image of the matrix and corresponding elemental mappings (**Figure 1**a) clearly show that Ag, Sb, and Mn atoms enter the Sn lattice sites. This is supported by the atom probe tomography (APT) data that show the 3D homogeneous distribution of elements Sn, Te, Sb, Mn, and Ag in Figure 1b. The nearest neighbor distribution function of atomic pairs between the same atoms, such as Sn-Sn, Te-Te, and Ag-Ag, is extracted from the APT reconstruction map. The experimental results (solid circles) are perfectly in line with the theoretical randomized binomial distributions (lines), confirming the absence of atomic clusters and other segregation effects in the probed volume of the APT specimen.[28] In contrast, we observed the Ag clustering effect in the matrix of a single Ag-doped SnTe and the average composition of Ag in the matrix is ≈0.5–0.7 at.% (See Figure S5, Supporting Information), consistent with the previous work.[22] Note that a high solubility of Ag in SnTe beyond 10 at.% has been reported,[21,29] but the value was derived from XRD measurement, which has a much lower detection resolution than APT.[30] The linear composition profile along the vertical direction of Figure 1b shows no composition fluctuations and gives a stoichiometry close to the nominal one ($Sn_{0.87}Mn_{0.08}Sb_{0.08}Te$–5%$AgSbTe_2$) except for 3 at.% Mn deficiency. The reason for this deficiency will be given later. The high solubility of these doping elements in SnTe is quite surprising and contrary to the high number density of Ag-rich nanoprecipitates observed in Ag/Mn co-doped SnTe.[19,20]

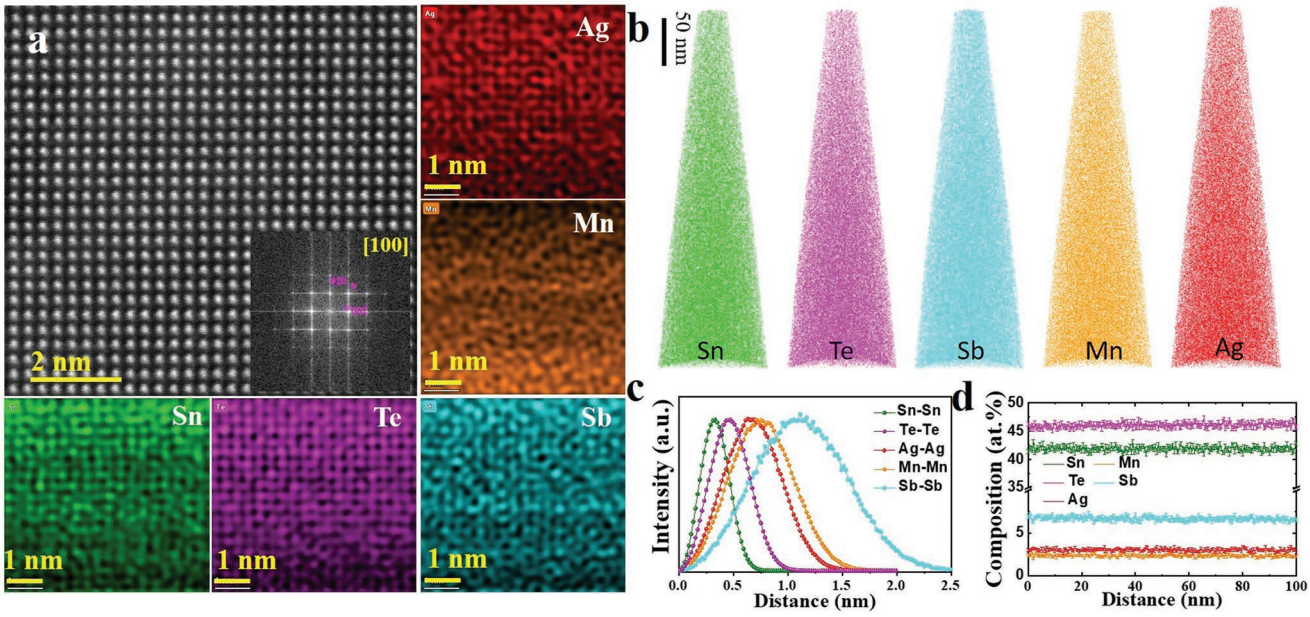

Figure 1. HAADF-STEM images and APT characterization of Sn0.87Mn0.08Sb0.08Te–5%AgSbTe2: a) Atomic-resolution HAADF-STEM image and EDS mappings of SnTe matrix (FFT image that corresponds to the HAADF-STEM image inset), b) 3D reconstruction showing the distribution of constituent elements, c) nearest-neighbor atomic distribution histograms of these five elements, d) Composition profile taken from a cuboid region of interest along the vertical direction over 100 nm in length.

The major difference between our samples and the Ag/Mn co-doped SnTe[19,20] appears at first sight to be the addition of Sb. We first analyze the impact of atomic size and electronegativity according to the Hume–Rothery rule. The Shannon radii for Ag, Mn, Sb, and Sn in octahedral coordination are 1.15, 0.67, 0.76, and 0.93 Å, respectively. The electronegativity for Ag, Mn, Sb, and Sn on the Pauling scale are 1.93, 1.55, 2.05, and 1.96, respectively. It seems that Ag should have a high solubility in SnTe given the small difference in atomic size and electronegativity between Ag and Sn, while experiments show the opposite.[22] Since both Mn and Sb show a smaller atomic size than that of Ag, the increased solubility by adding Sb can neither be attributed to the strain compensation effect due to size mismatch. One more argument could be the high-entropy effect. Yet, the increased configurational entropy by adding Sb cannot be fully responsible for the enlarged solubility of all elements. Note that a high number density of precipitates have been observed in $SnAg_{0.05}Te$-6%CdSe,[22] which should have a high configurational entropy by forming a solid solution. This interesting phenomenon that much more Ag can be dissolved in SnTe as $AgSbTe_2$ than as Ag calls for another explanation.

Besides the high spatial resolution and chemical sensitivity of APT, this technique has a unique attribute to capture the information of chemical bonding[31] endorsed by the high electric-field-induced bond breaking and atom evaporation during APT measurements.[30,32,33] For laser-assisted APT, an effective laser pulse can either trigger the evaporation of a single ion or multiple ions, which are called a single event and multiple events, respectively. The ratio of multiple events to the total events is called the "probability of multiple events (PME)". **Figure 2**a shows the PME map of SnTe, $AgSbTe_2$, SnTe-$AgSbTe_2$, and Ag-doped SnTe. A high PME (≈75%) value is observed in the former three compounds. In contrast, a big Ag_2Te precipitate is found in the Ag-doped SnTe sample exhibiting a much lower PME value (≈30%), in agreement with the work by Rodenkirchen et al.[34] It has been demonstrated that a high PME value (>60%) is characteristic and a hallmark of an unconventional bonding mechanism, called metavalent bonding (MVB).[31,35,36] In addition to the similarly high PME values for SnTe and $AgSbTe_2$, they share many common properties, such as a large optical dielectric constant, a small bandgap, a high effective coordination number, and a strong anharmonicity, which all are fingerprints of MVB.[37] This special property portfolio can be employed to design phase-change, thermoelectric materials,[34] tailor crystallization, and vitrification kinetics.[38] Moreover, the resulting solid solution of SnTe and $AgSbTe_2$ utilizes the same MVB mechanism, while the non-MVB Ag_2Te phase separates from the MVB SnTe matrix, as proved by the PME map. This implies that the improved solubility could originate from the coexistence of MVB in two compounds. Guarneri et al.[39] systematically studied the tie line between GeTe-GeSe and Sb_2Te_3-Sb_2Se_3, where the formers (GeTe and Sb_2Te_3) are MVB compounds and the latters are covalently bonded solids. They found phase separation and discontinuous changes in several physical and optical properties across the border between MVB and covalently bonded systems. The miscibility between different compounds can be roughly estimated from a chemical bonding map spanned by the value of electrons transferred and shared, as illustrated in Figure 2b.[34,35] This map shows a generic trend, if one analyzes phase diagrams where one component employs MVB, i.e., in the green region of the map. If the second component also utilizes MVB, good miscibility is accomplished, like the case for SnTe and $AgSbTe_2$. On the other hand, phase separation is typically encountered, when metavalent and covalent (ionic or metallic) solids are mixed, like the case for SnTe and Ag_2Te. This treasure map provides

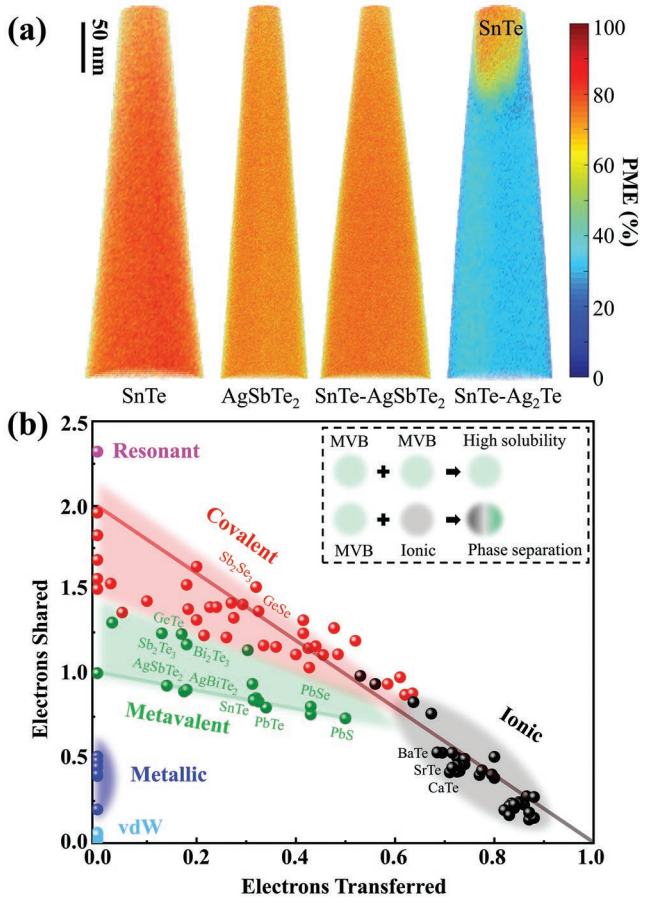

Figure 2. a) Probability of multiple events (PME) maps of different compounds characterized by APT. The last figure shows a big Ag_2Te precipitate (low PME) in the Ag-doped SnTe sample with a small part of the SnTe matrix (high PME) detected. b) 2D map describing chemical bonds in solids. The map is spanned by the number of electrons transferred normalized by the oxidation state and electrons shared between adjacent atoms. Different chemical bonding mechanisms are demarcated by different colors. Numerical data and detailed labels of all data points can be found in Ref. [35]. This map can be employed to design thermoelectrics where different dopant solubilities are desired.

a recipe to design thermoelectrics, where different levels of dopant solubilities are desired. For example, high-entropy thermoelectrics can be generated by alloying MVB compounds, e.g., high-entropy GeTe-PbTe-$AgSbTe_2$-$(Bi,Sb)_2Te_3$ alloy,[40] while nano-precipitates will be formed by alloying MVB compounds with covalent or ionic compounds, e.g., CaTe/BaTe (ionic) precipitates in PbTe (MVB).[41]

2.2. Energy Band Structures Modulated by Tuning Local Chemical Bonds

To elucidate the effects of Mn/Sb codoping and $AgSbTe_2$ alloying on the electrical properties of SnTe, we first studied the electronic band structures of the pristine SnTe in **Figure 3**a. The calculated band structures show a bandgap of 0.1 eV and an energy difference between L and Σ points (ΔE(L-Σ)) of 0.25 eV (**Table 1**), which are consistent with the previous study.[42] The VBM of pristine SnTe is mainly from the Sn−p and Te−p bonding with the addition of antibonding states between Sn−s and Te−p.[43] The strength of the VBM depends on the positions of atomic levels that can be tuned by chemical doping. Introducing intrinsic Sn vacancies ($Sn_{0.963}Te$, Figure 3b) in the supercell only shifts down the Fermi energy level into the valance band, resulting in a high hole concentration, while having no effects on the bandgap and ΔE(L-Σ) values (Table 1). In contrast, doping Mn/Sb into SnTe can significantly modify the band structures, especially the valence bands (Figure 3c/d). In comparison with the pristine SnTe, the 4% Mn/Sb co-doped SnTe ($Sn_{0.889}Mn_{0.037}Sb_{0.037}Te$ in Figure 3c) shows the increased bandgap from 0.10 to 0.17 eV and decreased ΔE(L-Σ) from 0.25 to 0.11 eV (Table 1). This suggests that the Mn/Sb codoping could suppress the bipolar effect and leads to notable convergence of the light and heavy valence bands. Increasing the Mn and Sb concentrations to 8%, the bandgap increases to 0.24 eV, and ΔE(L-Σ) further decreases to 0.02 eV (Table 1 and Figure 3d). This will further improve the band convergence, leading to the high density of states around the valence band maximum (VBM) (Figure S6, Supporting Information). To verify the dominant dopant (Sb or Mn) underpinning the bandgap enlargement and band convergence, we calculated the band structures under individual Sb or Mn doping with varied concentrations ($Sn_{0.926}Sb_{0.037}Te$ and $Sn_{0.889}Sb_{0.074}Te$, $Sn_{0.926}Mn_{0.037}Te$, and $Sn_{0.889}Mn_{0.074}Te$ in Figure S7, Supporting Information and the corresponding crystal structures in Figure S8, Supporting Information). It turns out that Sb doping does not evidently improve the bandgap and valley degeneracy (Table 1; Figure S7a,b, Supporting Information), but can tune the carrier concentration by providing electrons to compensate for the holes in the valence band (the Fermi energy level shifts upward compared to that of $Sn_{0.963}Te$, Figure S7b, Supporting Information). On the other hand, Mn doping significantly decreases ΔE(L-Σ) and increases the bandgap (Table 1; Figure S7c,d, Supporting Information). This suggests that the band alignment (very small ΔE(L-Σ) and large bandgap) for the Mn/Sb codoped SnTe compound is mainly contributed by Mn doping (**Figure 4**a). Introducing Ag in SnTe ($Sn_{0.926}Ag_{0.037}Te$, Figure 3e) can further decrease ΔE(L-Σ).[44] Interestingly, when increasing the Ag concentration to ≈7% ($Sn_{0.889}Ag_{0.074}Te$, Figure 3f), its VBM deviates from the original L point, but along the Γ-L line. The energy difference between the VBM and Σ-band is further decreased to 0.11 eV. Additionally, the VBM deviation will lift the deep valence band along the Γ-L line in the pristine SnTe compound (Figure 3a), which helps to align the valence bands of Mn and Sb doped SnTe (illustrated in Figure 4a). The existence of the VBM at the L point and the band convergence in rock-salt IV-VI compounds have been explained by the contribution of cation-s states that make up the valence band edge.[45] However, recent understandings from a tight-binding method reveal that the interaction between cation-p and anion-p states is sufficient to provide the molecular orbitals with the proper s-type symmetry to place the VBM at the L point.[46,47] Tan et al.[48] suggested a smaller difference between the s level of dopants and the p level of Te will induce a stronger band convergence in SnTe. The s energy levels for Mn and Ag are −5.5 and −4.73 eV, respectively, which are closer to the Te-p orbital (−6.12 eV) than that of Sn-s (−10.91 eV). As a consequence, the energy level at the L point

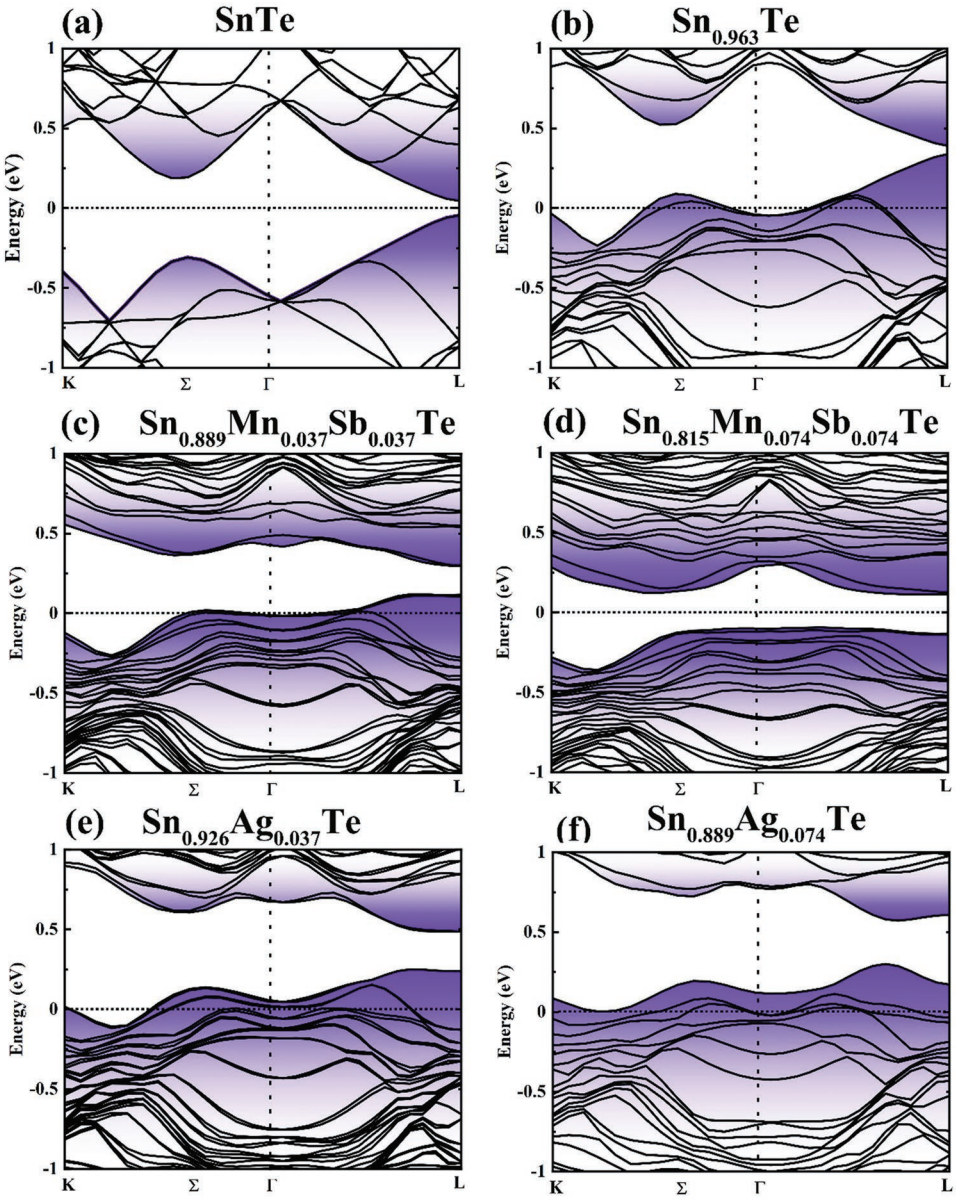

Figure 3. Electronic band structures of a) SnTe, b) $Sn_{0.963}Te$, c) $Sn_{0.889}Mn_{0.037}Sb_{0.037}Te$, d) $Sn_{0.815}Mn_{0.074}Sb_{0.074}Te$, e) $Sn_{0.926}Ag_{.037}Te$, f) $Sn_{0.889}Ag_{0.074}Te$.

decreases with the Mn and Ag doping, leading to an enlarged bandgap and band alignment.

2.3. Band Alignment Resulted from the Improved Solubility of Dopants

Figure 4b presents the electrical conductivity (σ) as a function of temperature for $Sn_{1.03-2x}Mn_xSb_xTe$–y%$AgSbTe_2$ samples. The σ of all samples decreases with increasing temperature, exhibiting a typical degenerate semiconductor behavior. Sn self-compensation can optimize the carrier concentration and thermoelectric performance by suppressing the intrinsic Sn vacancies.[49] Therefore, an additional 3 at.% Sn was introduced into the materials investigated, resulting in a reduction in carrier concentration and conductivity. σ decreases with increasing Mn and Sb content and reaches a minimum value for $x = 0.08$ sample. Such reduction of σ can be attributed to the decrease in carrier concentration (n_H) and carrier mobility (μ_H) induced by Mn and Sb codoping (Figure 4c1). Generally, Mn serves as an electron acceptor due to the reduced Sn vacancies formation energy.[50] The substitution of Sb at the Sn site provides extra electrons to compensate for the high hole carrier concentration, resulting in the reduction of carrier concentration. $Sn_{1.03-2x}Mn_xSb_xTe$ samples show reduced μ compared to that of pristine $Sn_{1.03}Te$ due to enhanced point defects scattering. σ slightly increases after alloying with $AgSbTe_2$, which can be ascribed to the enhanced carrier concentration from 1.96×10^{20} cm^{-3} for the $AgSbTe_2$ free sample to 5.9×10^{20} cm^{-3} for $Sn_{0.87}Mn_{0.08}Sb_{0.08}Te$–7%$AgSbTe_2$ (Figure 4c2). The Sn

Table 1. The bandgap and energy offset ΔE(L–Σ) between L and Σ points obtained by density functional theory calculations for SnTe, $Sn_{0.963}Te$, Mn and Sb codoped SnTe, Mn, Sb, Ag single-doped SnTe, respectively.

	ΔE(L–Σ) [eV]	Bandgap [eV]
SnTe	0.25	0.10
$Sn_{0.963}Te$	0.18	0.11
$Sn_{0.889}Mn_{0.037}Sb_{0.037}Te$	0.11	0.17
$Sn_{0.815}Mn_{0.074}Sb_{0.074}Te$	0.02	0.24
$Sn_{0.926}Sb_{0.037}Te$	0.23	0.05
$Sn_{0.889}Sb_{0.074}Te$	0.18	0.07
$Sn_{0.926}Mn_{0.037}Te$	0.12	0.21
$Sn_{0.889}Mn_{0.074}Te$	0.03	0.38
$Sn_{0.926}Ag_{0.037}Te$	0.15	0.20
$Sn_{0.889}Ag_{0.074}Te$	0.11	0.27

vacancy concentration increases due to the decreased formation energy of Sn vacancies when Ag and Sb are alloyed at the Sn sites, which gives rise to increased hole concentration.[51] The reduction of mobilities is mainly attributed to the enhancement of carrier effective mass in the heavy valence band and strengthened point defects scattering caused by $AgSbTe_2$ alloying.[42,52,53]

Figure 4d presents the temperature dependence of the Seebeck coefficient (S) for $Sn_{1.03-2x}Mn_xSb_xTe$–y%$AgSbTe_2$. It is worthy to note that the S is significantly improved from 130 μVK^{-1} for $Sn_{1.03}Te$ to 176 μVK^{-1} for $Sn_{0.91}Mn_{0.06}Sb_{0.06}Te$ at 873 K, as shown in Figure 4d. The Seebeck coefficients further increase after alloying with $AgSbTe_2$ although the hole concentrations increase simultaneously (Figure 4c2). To understand the mechanism for S enhancement, we calculate the Pisarenko relation between S and the carrier concentration (n_H) based on the two valence bands model as depicted in Figure 4e. The room temperature S as a function of n_H of $Sn_{1.03-2x}Mn_xSb_xTe$–y%$AgSbTe_2$ and those of other reported SnTe samples are compared. The data of $Sn_{1.03}Te$ and undoped SnTe,[54] Bi-doped,[55] and Cu-doped SnTe[56] match well with the theoretical Pisarenko line for the pristine SnTe with a ΔE(L-Σ) value of 0.35 eV (Figure 4e).[57] It was demonstrated that conventional element doping (Bi or Cu) plays a negligible effect on the band structure of SnTe.[54] In contrast, S values of Mn and Sb codoped samples lie above the prediction line due to the strong valence band convergence. It is worth noting that S values of $Sn_{0.87}Mn_{0.08}Sb_{0.08}Te$–y%$AgSbTe_2$ samples are even higher than that of Mn-Sb codoped SnTe. We also calculated the Pisarenko lines with varying valence energy offset ΔE(L-Σ) as shown in Figure 4e. The experimental values of $Sn_{0.87}Mn_{0.08}Sb_{0.08}Te$–y%$AgSbTe_2$ samples match well with the DFT calculations that Ag dopant results in reduced energy offset. This phenomenon indicates that the increased solubility of Ag in SnTe by alloying with MVB $AgSbTe_2$ leads to a stronger band convergence effect (band alignment).

The improvement of the Seebeck coefficient induced by band alignment contributes to the high-power factor (PF) (Figure 4f). For $Sn_{0.87}Mn_{0.08}Sb_{0.08}Te$–5%$AgSbTe_2$, a remarkable PF of 28.1 $\mu W\ cm^{-1}K^{-2}$ is obtained at 873 K, which is significantly enhanced compared with that of pure SnTe and $Sn_{1.03}Te$. The large integral area of PF for $Sn_{0.87}Mn_{0.08}Sb_{0.08}Te$–5%$AgSbTe_2$ demonstrates that our strategy can optimize the electrical transport properties over the whole temperature range (Figure S9, Supporting Information), benefiting the requirement of large output power in practical services.

2.4. Enhanced Phonon Scattering by Multi-Scale Structural Defects

Figure 5a shows the total thermal conductivity (κ_T) for $Sn_{1.03-2x}Mn_xSb_xTe$–y%$AgSbTe_2$ samples. The lattice thermal conductivity (κ_L) is calculated according to the formula $\kappa_L = \kappa_T - \kappa_e$, in which the charge carrier thermal conductivity κ_e is estimated based on the Wiedemann–Franz law ($\kappa_e = LT\sigma$) (Figure S10, Supporting Information). The Lorenz number (L) is evaluated from the temperature-dependent Seebeck coefficient with an assumption of a single-band model (Figure S11, Supporting Information).[20,57] Due to the phonon–phonon Umklapp scattering,[59] κ_L of all the samples reduces with increasing temperature. It is shown that Sn self-compensation $Sn_{1.03}Te$ exhibits lower κ_L than the pristine SnTe. κ_L of $Sn_{1.03-2x}Mn_xSb_xTe$ decreases with Mn and Sb doping levels and is significantly lower than that of the pure SnTe and $Sn_{1.03}Te$ samples. Moreover, κ_L can be further lowered by introducing $AgSbTe_2$. At 873 K, the lowest κ_L of 0.3 $Wm^{-1}\ K^{-1}$ is obtained for $Sn_{0.87}Mn_{0.08}Sb_{0.08}Te$–5%$AgSbTe_2$, which is lower than most of the reported SnTe-based thermoelectrics and below the theoretical amorphous limit (≈0.4 $Wm^{-1}\ K^{-1}$) of SnTe calculated from the Debye–Cahill model.[60] Introducing more $AgSbTe_2$ into the matrix cannot enhance the phonon scattering because the phonon mean free path has already reached its minimum.

It should be noted that point defect phonon scattering plays an important role in reducing κ_L due to the small phonon mean free path of SnTe.[61] The calculated results predict that point defect scattering (Mn, Sb substitution and $AgSbTe_2$ alloying) significantly reduces lattice thermal conductivity in SnTe (Figure 5c). Yet, nearly 20% of the cumulative lattice thermal conductivity is contributed by phonons with mean free paths longer than 20 nm.[62] Indeed, the experiment κ_L values in the whole temperature range for $Sn_{0.87}Mn_{0.08}Sb_{0.08}Te$–5%$AgSbTe_2$ are lower than the calculations by only taking point defects into account. To further understand the mechanism of the lowered κ_L, we characterized the microstructures of the $Sn_{0.87}Mn_{0.08}Sb_{0.08}Te$–5%$AgSbTe_2$ sample through atomic-resolution HAADF-STEM and annular bright-field (ABF) imaging modes. HAADF-STEM images (**Figure 6**a) show nanoprecipitates in the matrix with an average size of ≈10 nm. Figure 6b shows an enlarged HAADF-STEM image from Figure 6a highlighting the nanoprecipitates. The STEM-EDS elemental mappings (Figures 6b1–b5) and the atomic-resolution HAADF-STEM images (Figure S12, Supporting Information) confirm Mn enrichment at the precipitates. APT results show a composition of Mn of ≈5 at.% in the matrix. This value is much lower than 13 at.% solubility limit of Mn in SnTe obtained by XRD.[63] Yet, APT has a much higher elemental sensitivity and composition accuracy (ppm level) than XRD.[30] Thus, the true solubility of Mn in SnTe should be reevaluated as ≈5 at.%. Extra Mn will form precipitates but cannot be detected

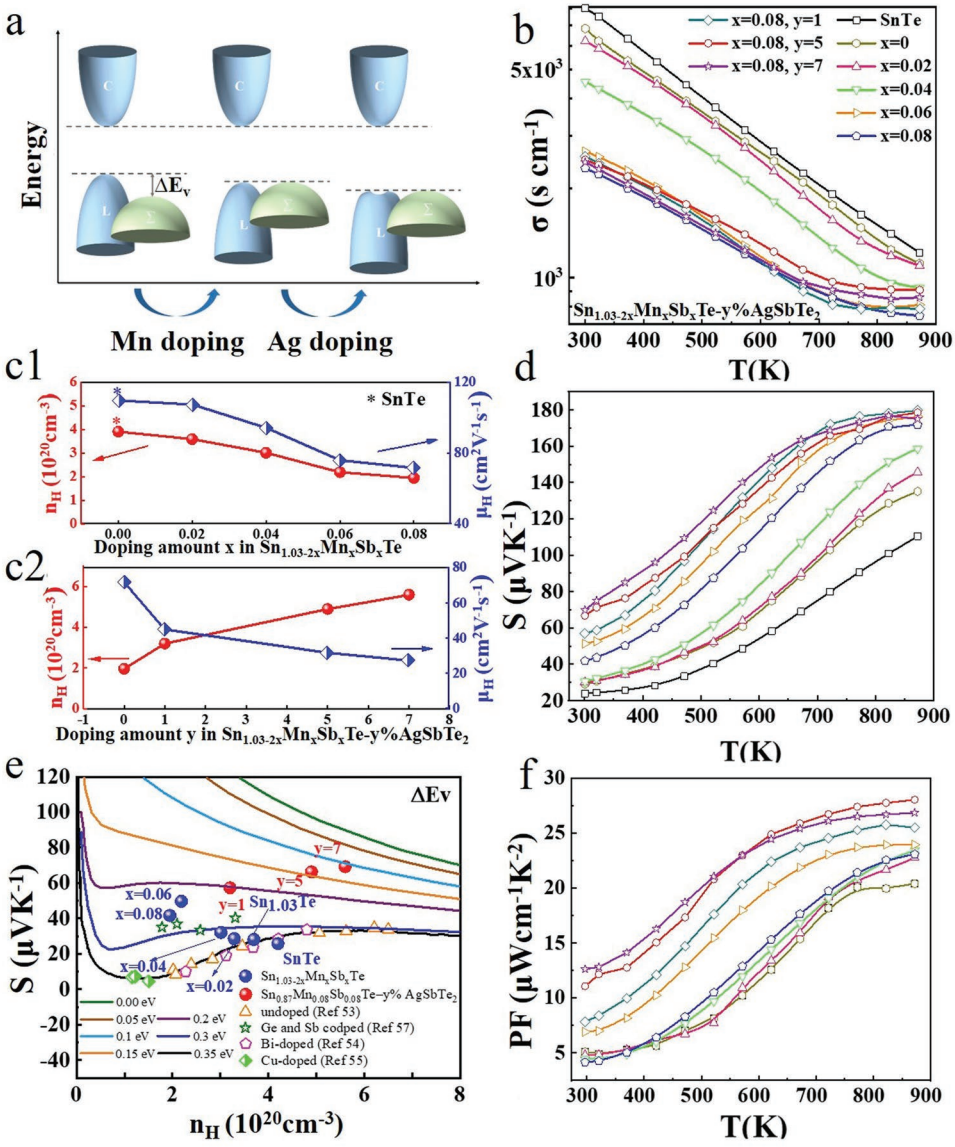

Figure 4. Energy band structures and electrical transport properties of $Sn_{1.03-2x}Mn_xSb_xTe$–y%$AgSbTe_2$ samples: a) The schematic illustration of band structure change upon Mn and Ag doping. b) Electrical conductivity, c1–c2) Compositional dependence of the carrier concentration n_H and the carrier mobility μ_H at room temperature, d) Seebeck coefficient, e) Room temperature Seebeck coefficients as a function of the carrier concentration. For comparison, previously reported data of undoped SnTe,[54] Bi-doped,[55] Cu-doped,[56] and Ge-Sb codoped[58] SnTe samples, as well as theoretical Pisarenko curves based on the two-valence-band model with varying valence band offset (ΔE(L-Σ)). f) Power factor.

by XRD due to the limited resolution. The smaller solubility of Mn than that of Ag and Sb in the SnTe matrix could also be explained from a chemical bonding perspective because MnTe is a non-MVB compound while both $AgSbTe_2$ and SnTe utilize MVB. Figure 6c presents a typical incoherent interface between the Mn-rich nanoprecipitate and the SnTe matrix, which can be attributed to the relatively large lattice mismatch (≈28%). Besides the precipitates, HAADF-STEM (Figure 6e) shows typical dislocation arrays. The atomic arrangements around a dislocation core are further revealed in Figure 6e. Combined with the inset FFT image and the Burgers loop, the projected Burgers vector of the partial dislocation line can be confirmed as 1/2[001_]. Dislocations and Mn-rich nanoprecipitates provide extra phonon scattering sources leading to decreased κ_L for the $Sn_{0.87}Mn_{0.08}Sb_{0.08}Te$–5%$AgSbTe_2$ sample. We also compared the grain size of sample $Sn_{0.87}Mn_{0.08}Sb_{0.08}Te$ (8.07 μm) and sample $Sn_{0.87}Mn_{0.08}Sb_{0.08}Te$–5%$AgSbTe_2$ (8.52 μm) in Figure S13 (Supporting Information). Negligible difference in grain size can be observed for both samples, indicating that the further lowered lattice thermal conductivity by alloying $AgSbTe_2$ is not due to grain boundary phonon scattering.[64]

The XRD results (Figures S14a–b, Supporting Information) show a broadening and a decrease in intensity of the diffraction peaks, indicative of lattice strains in the $Sn_{0.87}Mn_{0.08}Sb_{0.08}Te$–5%$AgSbTe_2$ sample.[65] The lattice strains are estimated to be 0.57% using the full-width half-maximum

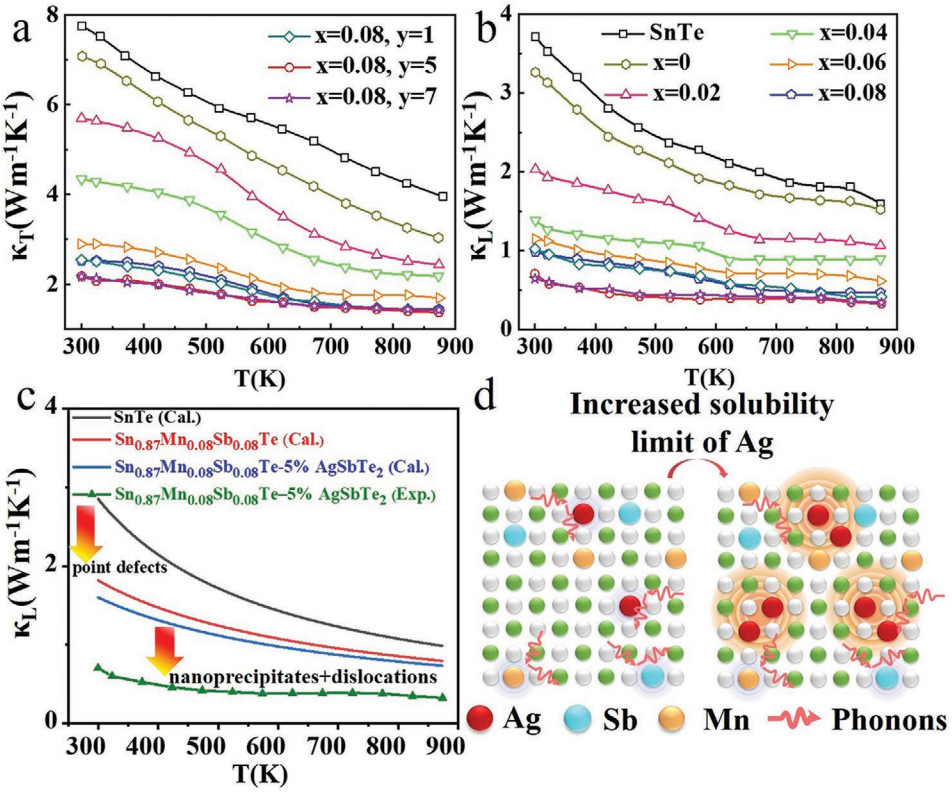

Figure 5. Thermal transport properties of $Sn_{1.03-2x}Mn_xSb_xTe$–y%$AgSbTe_2$ as a function of temperature and schematic illustration of reinforcing phonon scattering by enhanced point defect in SnTe: a) total thermal conductivity, b) lattice thermal conductivity, c) calculated lattice thermal conductivity using the Debye–Callaway model in the whole temperature region for the pristine SnTe and compounds with different alloying elements; the experimental κ_L value of $Sn_{0.87}Mn_{0.08}Sb_{0.08}Te$–5%$AgSbTe_2$ is provided for comparison, d) schematic illustration of reinforcing phonon scattering by increased point defects in SnTe.

(FWHM) method (Figures S14c–d, Supporting Information). Such a large strain value should stem from both point defects and dislocations. The high content of point defects (Mn, Sb, and Ag substitution) induces large lattice strains in SnTe due to mismatched atomic sizes. While the local strain around dislocations can be spatially mapped by the geometric phase analysis (GPA) (Figure 6f). These lattice strains can soften phonons, leading to a significant reduction in κ_L.[66–68] Therefore, the increased solubility of dopants induces stronger point defect phonon scattering and softening, which plays a dominant role in reducing κ_L (illustrated in Figure 5d).

2.5. Exceptional Thermoelectric Figure of Merit *ZT*

Figure 7a shows the temperature-dependent *ZT* for $Sn_{1.03-2x}Mn_xSb_xTe$–y%$AgSbTe_2$ samples. *ZT* of Sn self-compensated $Sn_{1.03}Te$ is enhanced compared to pure SnTe due to the optimization of carrier concentration. Mn and Sb codoping can efficiently enhance *ZT* thanks to the optimized electrical transport property and reduced κ_T, increasing the *ZT* value from 0.60 for $Sn_{1.03}Te$ to 1.4 for $Sn_{0.87}Mn_{0.08}Sb_{0.08}Te$. *ZT* can be further enhanced through alloying with $AgSbTe_2$. An ultrahigh peak *ZT* of ≈1.8 is achieved in $Sn_{0.87}Mn_{0.08}Sb_{0.08}Te$–5%$AgSbTe_2$ at 873 K, showing 180% enhancement compared with $Sn_{1.03}Te$. This value outperforms most of the reported SnTe-based systems (Figure 7b).[69–74] Multiple measurements confirm that such high performance is highly stable and repeatable (Figures S15–S16, Supporting Information). Achieving a large average *ZT* in a wide temperature range is greatly desired for enhancing thermoelectric conversion efficiency. Average *ZT* (ZT_{ave}) can be calculated according to the formula:

$$ZT_{ave} = \frac{1}{T_h - T_c}\int_{T_c}^{T_h} ZT dT \quad (1)$$

It is worth noting that a remarkable ZT_{ave} of ≈1.0 can be achieved in $Sn_{0.87}Mn_{0.08}Sb_{0.08}Te$–5%$AgSbTe_2$ over a wide temperature range (400–873 K), which is a record-high value for SnTe-based compounds. A large ZT_{ave} can yield a high theoretical energy conversion efficiency η:[75]

$$\eta = \frac{T_h - T_c}{T_h}\left[\frac{\sqrt{1+ZT_{ave}}-1}{\sqrt{1+ZT_{ave}}+T_c/T_h}\right] \quad (2)$$

The above results prove that large peak and average *ZT* values can be achieved by combining band alignment and phonon engineering. These beneficial effects stem from the considerably increased solubility limit of dopants obtained by alloying two compounds characterized by metavalent bonding.

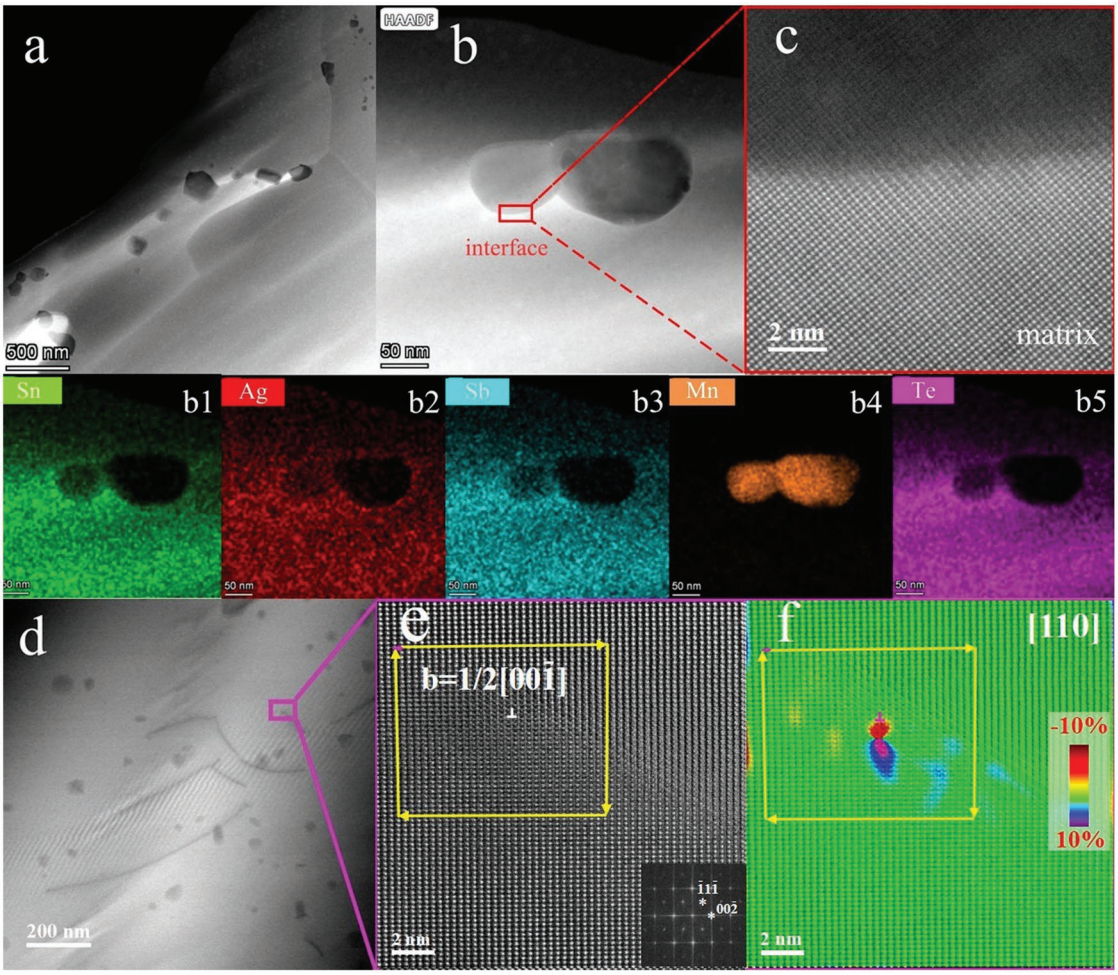

Figure 6. Microstructural characterizations of $Sn_{0.87}Mn_{0.08}Sb_{0.08}Te$–5%$AgSbTe_2$: a) low magnification HAADF-STEM images of precipitates, b) HAADF-STEM image of one Mn-rich nanoprecipitate, b1–b5) EDS mappings taken from (b), and c) High-magnification HAADF-STEM image of the interface between Mn-rich precipitate and SnTe matrix (the bright contrast); d) ABF-STEM images showing the dislocations (the darker lines), e) Atomic-resolution HAADF-STEM image of the disappearing area of the dislocation line (with FFT image inset), and f) Strain mapping corresponding to the HRTEM image using the geometrical phase analysis (the color bar at the right indicates –10–10% strain range).

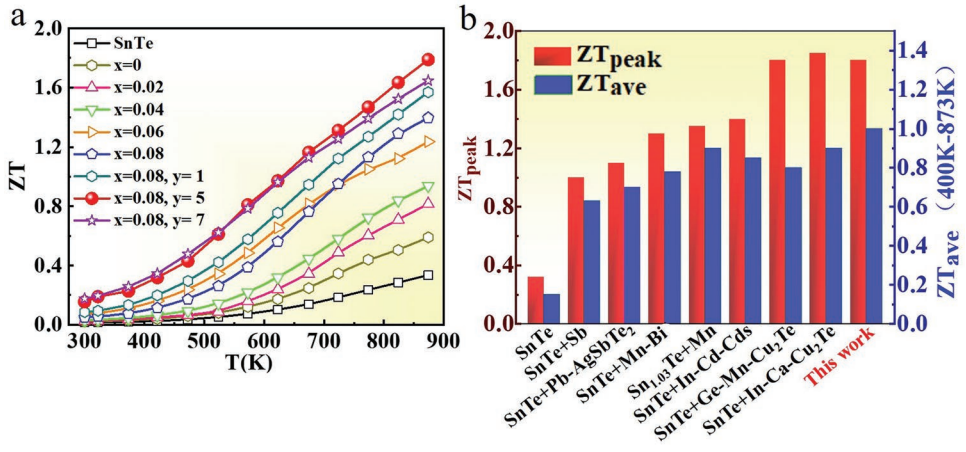

Figure 7. a) *ZT* of $Sn_{1.03-2x}Mn_xSb_xTe$–y%$AgSbTe_2$ as a function of temperature; b) Comparison of ZT_{peak} and ZT_{ave} of $Sn_{0.87}Mn_{0.08}Sb_{0.08}Te$–5%$AgSbTe_2$ with other reported SnTe systems.[51,69–72,76]

3. Conclusions

In summary, we demonstrated a new mechanism to increase the solubility of dopants by alloying compounds adopting the same metavalent bonding. The bond-rupture behavior characterized by APT proved the MVB nature in both SnTe and $AgSbTe_2$, while Ag_2Te is a non-MVB compound. Due to the coexistence of MVB in SnTe and $AgSbTe_2$, the solubility of Ag in SnTe was increased from 0.5 at.% to above 7 at.%. The sharp increase in solubility of dopants contributes to band alignment in SnTe, leading to a significantly enhanced Seebeck coefficient and power factor in the whole temperature range measured. Simultaneously, the increased solubility induces stronger point defect phonon scattering and softening, which plays a dominant role in reducing κ_L. The enhanced phonon scattering by point defects and associated lattice strain contributes to an extremely low κ_L of 0.30 Wm^{-1} K^{-1}. Consequently, a remarkable peak ZT value of 1.8 at 873 K and a record-high average ZT of ≈1.0 between 400 and 873 K are achieved in SnTe, enabling this SnTe-based alloy one of the best medium-temperature thermoelectric materials. We demonstrate that high thermoelectric performance can be realized through increasing the solubility of dopants by alloying compounds both employing MVB. Our findings not only open up a great opportunity for designing prospective materials for thermoelectric applications, but also provide a perspective for solubility improvement of materials.

Supporting Information

Supporting Information is available from the Wiley Online Library or from the author.

Acknowledgements

Y.L., X.Z., and P.N. contributed equally to this work. The work was supported by the National Natural Science Foundation of China (Nos. 52071182 and 11774347), "Qinglan Project" of the Young and Middle-aged Academic Leader of Jiangsu Province, the Fundamental Research Funds for the Central Universities (No. 30921011107), and the University Synergy Innovation Program of Anhui Province (No.GXXT-2020-003). Y.Y., O.C.-M., and M.W. acknowledge the financial support from DFG SFB 917 project. Y.Y. acknowledges the financial support under the Excellence Strategy of the Federal Government and the Länder within the ERS RWTH Start-Up grant (Grant No. StUpPD_392-21).

Open access funding enabled and organized by Projekt DEAL.

Conflict of Interest

The authors declare no conflict of interest.

Data Availability Statement

The data that support the findings of this study are available from the corresponding author upon reasonable request.

Keywords

band alignments, materials designs, metavalent bonding, solubility limits, thermoelectric

Received: August 29, 2022
Revised: September 9, 2022
Published online: September 25, 2022

[1] J. Tzer-Ming, T. Sheng-Chung, *App. Mech. Mater.* **2013**, *284*, 713.
[2] L. E. Bell, *Science* **2008**, *321*, 1457.
[3] G. Tang, J. Liu, J. Zhang, D. Li, K. H. Rara, R. Xu, W. Lu, J. Liu, Y. Zhang, Z. Peng, *ACS. Appl. Mater. Interfaces* **2018**, *10*, 30558.
[4] Y. Pei, X. Shi, A. LaLonde, H. Wang, L. Chen, G. J. Snyder, *Nature* **2011**, *473*, 66.
[5] A. D. LaLonde, Y. Pei, G. J. Snyder, *Energy Environ. Sci.* **2011**, *4*, 2090.
[6] X. Liu, T. Zhu, H. Wang, L. Hu, H. Xie, G. Jiang, G. J. Snyder, X. Zhao, *Adv. Energy Mater.* **2013**, *3*, 1238.
[7] H. Deng, X. Lou, W. Lu, J. Zhang, D. Li, S. Li, Q. Zhang, X. Zhang, X. Chen, D. Zhang, Y. Zhang, G. Tang, *Nano Energy* **2021**, *81*, 105649.
[8] M. Hong, Z.-G. Chen, L. Yang, Z.-M. Liao, Y.-C. Zou, Y.-H. Chen, S. Matsumura, J. Zou, *Adv. Energy Mater.* **2018**, *8*, 1702333.
[9] J. P. Heremans, V. Jovovic, E. S. Toberer, A. Saramat, K. Kurosaki, A. Charoenphakdee, S. Yamanaka, G. J. Snyder, *Science* **2008**, *321*, 554.
[10] W. Li, Y. Wu, S. Lin, Z. Chen, J. Li, X. Zhang, L. Zheng, Y. Pei, *ACS Energy Lett.* **2017**, *2*, 2349.
[11] C. Chang, Y. Liu, S. Lee, M. C. Spadaro, K. M. Koskela, T. Kleinhanns, T. Costanzo, J. Arbiol, R. L. Brutchey, M. Ibáñez, *Angew. Chem. Int. Ed.* **2022**, *61*, e202207002.
[12] W. Li, L. Zheng, B. Ge, S. Lin, X. Zhang, Z. Chen, Y. Chang, Y. Pei, *Adv. Mater.* **2017**, *29*, 1521.
[13] R. Moshwan, L. Yang, J. Zou, Z.-G. Chen, *Adv. Funct. Mater.* **2017**, *27*, 1703278.
[14] X. Zhang, D. Wang, H. Wu, M. Yin, Y. Pei, S. Gong, L. Huang, S. J. Pennycook, J. He, L.-D. Zhao, *Energy Environ. Sci.* **2017**, *10*, 2420.
[15] T. Fu, J. Xin, T. Zhu, J. Shen, T. Fang, X. Zhao, *Sci. Bull.* **2019**, *64*, 1024.
[16] G. Tan, F. Shi, J. W. Doak, H. Sun, L.-D. Zhao, P. Wang, C. Uher, C. Wolverton, V. P. Dravid, M. G. Kanatzidis, *Energy Environ. Sci.* **2015**, *8*, 267.
[17] Z. Chen, X. Guo, J. Tang, F. Xiong, W. Li, Y. Chen, R. Ang, *ACS Appl. Mater. Interfaces* **2019**, *11*, 26093.
[18] R. Al Rahal Al Orabi, N. A. Mecholsky, J. Hwang, W. Kim, J.-S. Rhyee, D. Wee, M. Fornari, *Chem. Mater.* **2016**, *28*, 376.
[19] R. Pathak, D. Sarkar, K. Biswas, *Angew. Chem., Int. Ed.* **2021**, *133*, 17827.
[20] D. Sarkar, T. Ghosh, A. Banik, S. Roychowdhury, D. Sanyal, K. Biswas, *Angew. Chem., Int. Ed.* **2020**, *59*, 11115.
[21] L. Zhao, J. Wang, J. Li, J. Liu, C. Wang, J. Wang, X. Wang, *Phys. Chem. Chem. Phys.* **2019**, *21*, 17978.
[22] D. An, J. Wang, J. Zhang, X. Zhai, Z. Kang, W. Fan, J. Yan, Y. Liu, L. Lu, C.-L. Jia, M. Wuttig, O. Cojocaru-Mirédin, S. Chen, W. Wang, G. J. Snyder, Y. Yu, *Energy Environ. Sci.* **2021**, *14*, 5469.
[23] J. Tang, B. Gao, S. Lin, X. Wang, X. Zhang, F. Xiong, W. Li, Y. Chen, Y. Pei, *ACS Energy Lett.* **2018**, *3*, 1969.
[24] U. Mizutani, *MRS Bull.* **2012**, *37*, 169.
[25] O. Senkov, J. Miller, D. Miracle, C. Woodward, *CALPHAD: Comput. Coupling Phase Diagrams Thermochem.* **2015**, *50*, 32.
[26] D. Bhat, U. Shenoy, *Mater. Today Phys.* **2019**, *11*, 100158.

[27] E. Quarez, K. F. Hsu, R. Pcionek, N. Frangis, E. K. Polychroniadis, M. G. Kanatzidis, *J. Am. Chem. Soc.* **2005**, *127*, 9177.
[28] T. Philippe, F. D. Geuser, S. Duguay, W. Lefebvre, O. Cojocarumirédin, G. D. Costa, D. Blavette, *Ultramicroscopy* **2009**, *109*, 1304.
[29] Y. Mizuguchi, O. Miura, *J. Phys. Soc. Jpn.* **2016**, *85*, 053702.
[30] Y. Yu, C. Zhou, S. Zhang, M. Zhu, M. Wuttig, C. Scheu, D. Raabe, G. J. Snyder, B. Gault, O. Cojocaru-Mirédin, *Mater. Today* **2020**, *32*, 260.
[31] S. Maier, S. Steinberg, Y. Cheng, C. F. Schön, M. Schumacher, R. Mazzarello, P. Golub, R. Nelson, O. Cojocaru-Mirédin, J. Y. Raty, M. Wuttig, *Adv. Mater.* **2020**, *32*, 2005533.
[32] B. Gault, A. Chiaramonti, O. Cojocaru-Mirédin, P. Stender, R. Dubosq, C. Freysoldt, S. K. Makineni, T. Li, M. Moody, J. M. Cairney, *Nat. Rev. Methods Primers* **2021**, *1*, 51.
[33] O. Cojocaru-Miredin, L. Abdellaoui, M. Nagli, S. Zhang, Y. Yu, C. Scheu, D. Raabe, M. Wuttig, Y. Amouyal, *ACS Appl. Mater. Interfaces* **2017**, *9*, 14779.
[34] B. J. Kooi, M. Wuttig, *Adv. Mater.* **2020**, *32*, 1908302.
[35] Y. Yu, M. Cagnoni, O. Cojocaru-Mirédin, M. Wuttig, *Adv. Funct. Mater.* **2020**, *30*, 1904862.
[36] C. Rodenkirchen, M. Cagnoni, S. Jakobs, Y. Cheng, J. Keutgen, Y. Yu, M. Wuttig, O. Cojocaru-Mirédin, *Adv. Funct. Mater.* **2020**, *30*, 1910039.
[37] M. Wuttig, V. L. Deringer, X. Gonze, C. Bichara, J. Y. Raty, *Adv. Mater.* **2018**, *30*, 1803777.
[38] C. Persch, M. Müller, A. Yadav, J. Pries, N. Honné, P. Kerres, S. Wei, H. Tanaka, P. Fantini, E. Varesi, F. Pellizzer, M. Wuttig, *Nat. Commun.* **2021**, *12*, 4978.
[39] L. Guarneri, S. Jakobs, A. V. Hoegen, S. Maier, M. Xu, M. Zhu, S. Wahl, C. Teichrib, Y. Zhou, O. Cojocaru-Mirédin, M. Raghuwanshi, C. F. Schön, M. Drögeler, C. Stampfer, R. P. S. M. Lobo, A. Piarristeguy, A. Pradel, J. Y. Raty, M. Wuttig, *Adv. Mater.* **2020**, *33*, 2102356.
[40] B. Jiang, W. Wang, S. Liu, Y. Wang, C. Wang, Y. Chen, L. Xie, M. Huang, J. He, *Science* **2022**, *377*, 208.
[41] K. Biswas, J. He, G. Wang, S.-H. Lo, C. Uher, V. P. Dravid, M. G. Kanatzidis, *Energy Environ. Sci.* **2011**, *4*, 4675.
[42] X. J. Tan, H. Z. Shao, J. He, G. Q. Liu, J. T. Xu, J. Jiang, H. C. Jiang, *Phys. Chem. Chem. Phys.* **2016**, *18*, 7141.
[43] X. Zhang, Z. Wang, B. Zou, M. K. Brod, J. Zhu, T. Jia, G. Tang, G. J. Snyder, Y. Zhang, *Chem. Mater.* **2021**, *33*, 9624.
[44] H. L. Min, D. G. Byeon, J. S. Rhyee, B. Ryu, *J. Mater. Chem. A* **2016**, *6*, 2235.
[45] W. G. Zeier, A. Zevalkink, Z. M. Gibbs, G. Hautier, M. G. Kanatzidis, G. J. Snyder, *Angew. Chem. Int. Ed.* **2016**, *55*, 6826.
[46] M. K. Brod, M. Y. Toriyama, G. J. Snyder, *Chem. Mater.* **2020**, *32*, 9771.
[47] M. Cagnoni, D. Fuehren, M. Wuttig, *Adv. Mater.* **2018**, *30*, 1801787.
[48] X. Tan, H. Wang, G. Liu, J. G. Noudem, H. Hu, J. Xu, H. Shao, J. Jiang, *Mater. Today Phys* **2018**, *7*, 35.
[49] G. J. Tan, L. D. Zhao, F. Y. Shi, J. W. Doak, S. H. Lo, H. Sun, C. Wolverton, V. P. Dravid, C. Uher, M. G. Kanatzidis, *J. Am. Chem. Soc.* **2014**, *136*, 7006.
[50] F. Guo, B. Cui, Y. Liu, X. Meng, J. Cao, Y. Zhang, R. He, W. Liu, H. Wu, S. J. Pennycook, W. Cai, J. Sui, *Small* **2018**, *14*, 1802615.
[51] G. Tan, S. Hao, R. C. Hanus, X. Zhang, S. Anand, T. P. Bailey, A. J. E. Rettie, X. Su, C. Uher, V. P. Dravid, G. J. Snyder, C. Wolverton, M. G. Kanatzidis, *ACS Energy Lett.* **2018**, *3*, 705.
[52] Y. Pei, H. Wang, G. J. Snyder, *Adv. Mater.* **2012**, *24*, 6125.
[53] T. Wang, H. Wang, W. Su, J. Zhai, X. Wang, T. Chen, C. Wang, *J. Mater. Sci.* **2019**, *54*, 9049.
[54] R. F. Brebrick, A. J. Strauss, *Phys. Rev.* **1963**, *132*, 104.
[55] L.-D. Zhao, X. Zhang, H. Wu, G. Tan, Y. Pei, Y. Xiao, C. Chang, D. Wu, H. Chi, L. Zheng, S. Gong, C. Uher, J. He, M. G. Kanatzidis, *J. Am. Chem. Soc.* **2016**, *138*, 2366.
[56] Y. Pei, L. Zheng, W. Li, S. Lin, Z. Chen, Y. Wang, X. Xu, H. Yu, Y. Chen, B. Ge, *Adv. Electron. Mater.* **2016**, *2*, 1600019.
[57] Q. Zhang, B. L. Liao, Y. C. Lan, K. Lukas, W. S. Liu, K. Esfarjani, C. Opeil, D. Broido, G. Chen, Z. F. Ren, *Proc. Natl. Acad. Sci. USA* **2013**, *110*, 13261.
[58] X. Li, J. Liu, S. Li, J. Zhang, D. C. Li, R. Xu, Q. Zhang, X. Zhang, B. Xu, Y. Zhang, F. Xu, G. Tang, *Nano Energy* **2020**, *67*, 104261.
[59] J. Liu, P. Wang, M. Wang, R. Xu, J. Zhang, J. Liu, D. Li, N. Liang, Y. Du, G. Chen, G. Tang, *Nano Energy* **2018**, *53*, 683.
[60] D. G. Cahill, S. K. Watson, R. O. Pohl, *Phys. Rev. B* **1992**, *46*, 6131.
[61] S. Roychowdhury, R. K. Biswas, M. Dutta, S. K. Pati, K. Biswas, *ACS Energy Lett.* **2019**, *4*, 1658.
[62] S. Lee, K. Esfarjani, T. Luo, J. Zhou, Z. Tian, G. Chen, *Nat. Commun.* **2014**, *5*, 3525.
[63] H. Wu, C. Chang, D. Feng, Y. Xiao, X. Zhang, Y. Pei, L. Zheng, S. Gong, D. Wu, Y. Chen, J. He, M. G. Kanatzidis, L.-D. Zhao, *Energy Environ. Sci.* **2015**, *8*, 3298.
[64] F. Zhang, D. Wu, J. He, *Mater. Lab* **2022**, *1*, 220012.
[65] A. K. Zak, W. H. A. Majid, M. E. Abrishami, R. Yousefi, *Solid State Sci.* **2011**, *13*, 251.
[66] Y. Wu, Z. Chen, P. Nan, F. Xiong, S. Lin, X. Zhang, Y. Chen, L. Chen, B. Ge, Y. Pei, *Joule* **2019**, *3*, 1276.
[67] X. Lou, S. Li, X. Chen, Q. Zhang, H. Deng, J. Zhang, D. Li, X. Zhang, Y. Zhang, H. Zeng, G. Tang, *ACS Nano* **2021**, *15*, 8204.
[68] R. Hanus, T. Matthias, J. E. Alexander, Z. Chen, D. Y. Chung, G. Tan, G. K. Mercouri, Y. Pei, W. V. Peter, G. J. Snyder, *Adv. Mater.* **2019**, *31*, 1900108.
[69] A. Banik, B. Vishal, S. Perumal, R. Datta, K. Biswas, *Energy Environ. Sci.* **2016**, *9*, 2011.
[70] Q. Zhang, X. Tan, Z. Guo, H. Wang, C. Xiong, N. Man, F. Shi, H. Hu, G.-Q. Liu, J. Jiang, *Chem. Eng. J.* **2021**, *421*, 127795.
[71] G. Tan, F. Shi, S. Hao, H. Chi, L.-D. Zhao, C. Uher, C. Wolverton, V. P. Dravid, M. G. Kanatzidis, *J. Am. Chem. Soc.* **2015**, *137*, 5100.
[72] T. Hong, D. Wang, X. B. Qin, Y. C. Zhang, X. Gao, L.-D. Zhao, *Mater. Today Phys.* **2021**, *21*, 100505.
[73] J. Tang, B. Gao, S. Lin, J. Li, Z. Chen, F. Xiong, W. Li, Y. Chen, Y. Pei, *Adv. Funct. Mater.* **2018**, *28*, 1803586.
[74] T. Hussain, X. Li, M. H. Danish, M. U. Rehman, J. Zhang, D. Li, G. Chen, G. Tang, *Nano Energy* **2020**, *73*, 104832.
[75] L.-D. Zhao, G. Tan, S. Hao, J. He, Y. Pei, H. Chi, H. Wang, S. Gong, H. Xu, V. P. Dravid, C. Uher, G. J. Snyder, C. Wolverton, M. G. Kanatzidis, *Science* **2016**, *351*, 141.
[76] G. Tan, F. Shi, H. Sun, L.-D. Zhao, C. Uher, V. P. Dravid, M. G. Kanatzidis, *J. Mater. Chem. A* **2014**, *2*, 20849.